



## Simulating particle settling in inclined narrow channels with the unresolved CFD-DEM method

Junsheng Zeng <sup>1</sup>, Pengfei Tang,<sup>2</sup> Heng Li,<sup>3</sup> and Dongxiao Zhang <sup>4,\*</sup>

<sup>1</sup>*Intelligent Energy Laboratory, Frontier Research Center, Peng Cheng Laboratory, Shenzhen 518000, People's Republic of China*

<sup>2</sup>*Energy and Resources Engineering, College of Engineering, Peking University, Beijing 100871, People's Republic of China*

<sup>3</sup>*School of Earth Resources, China University of Geosciences, Wuhan 730074, People's Republic of China*

<sup>4</sup>*School of Environmental Science and Engineering, Southern University of Science and Technology, Shenzhen 518055, People's Republic of China*



(Received 11 August 2020; accepted 8 March 2021; published 26 March 2021)

Acceleration of particle settling in inclined containers, known as the Boycott effect, is a common natural phenomenon, which can significantly affect the particle conveying process. Particularly for proppant transport constrained in narrow channels, physical mechanisms related to this effect remain undetermined. In this study, an Eulerian-Lagrangian method, i.e., the unresolved computational fluid dynamics–discrete element method, has been adopted to simulate the particle settling process in inclined narrow channels, with an aim to deepen the understanding of the Boycott effect on proppant settling. The simulation results illustrate that two types of granular-induced instabilities dominate the sediment settling process in inclined fractures, which are analogous to Kelvin-Helmholtz instability and Rayleigh-Taylor instability, respectively. Due to the instabilities, spatial inhomogeneity of the particle phase, i.e., particle clustering, is clearly observed. Based on parametric studies, it is proven that there exists a critical inclination angle where the acceleration ratio reaches a maximum, which ranges from 2 to 6 in this work. Moreover, the critical angle can shift between  $60^\circ$  and  $75^\circ$  as physical properties change, such as fluid viscosity, particle size, and particle density.

DOI: [10.1103/PhysRevFluids.6.034302](https://doi.org/10.1103/PhysRevFluids.6.034302)

### I. INTRODUCTION

Acceleration of particle settling in inclined containers is a common natural phenomenon in energy and resources engineering, and is often referred to as the Boycott effect [1,2]. In water treatment engineering, this effect is usually utilized for effective sand settlement in Lamella gravity settlers [3,4]. However, this effect is undesired for the proppant transport process in hydraulic fracturing systems [5,6], which is essentially a two-phase flow with strong fluid-particle coupling constrained in narrow channels. The Boycott effect may negatively affect the proppant transport distance in stimulated fracture networks due to the undesired rapid settling.

Although the Boycott effect is significant for proppant transport, it is seldom investigated and usually overlooked in extant literature. In previous works, stimulated fractures are frequently considered as vertical, assuming that fractures propagate perpendicular to the direction of minimum horizontal stress [7]. However, for existing natural fractures, the directions are more complex due to long-term stratigraphic evolutions [8]. When hydraulic fractures intersect with natural fractures,

---

\*zhangdx@sustech.edu.cn

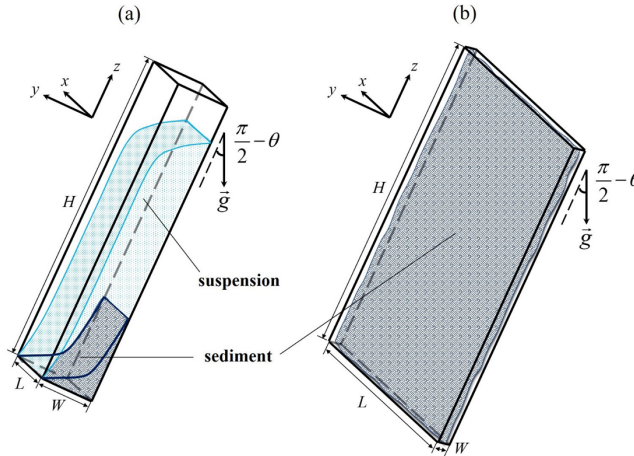


FIG. 1. Illustration of particle settling in an inclined vessel (a) and in an inclined fracture or narrow channel (b).  $L$ ,  $W$ , and  $H$  denote horizontal spreading length, transverse width, and longitudinal height of vessel or fracture in the  $x$ ,  $y$ , and  $z$  directions, respectively.  $\vec{g}$  is the gravity in the vertical direction, and  $\theta$  is the inclination angle. Note that  $\theta = \pi/2$  indicates a rigorously vertical state.

considering the effects of fracture inclination on proppant settling becomes significant. Recently, Chun *et al.* [9] studied proppant transport in inclined fractures through experimental approaches, and reported that sand dunes actually build up faster in an inclined fracture. Therefore, it is crucial to elucidate the underlying physical mechanisms for deepening the understanding of the Boycott effect on particle settling in inclined narrow channels, and find a feasible solution for suppressing the Boycott effect for proppant transport.

The Boycott effect was first identified by Boycott [10] when studying the sedimentation of blood corpuscles in inclined tubes. Particle settling in inclined vessels [Fig. 1(a)] has been investigated for several decades, with corresponding models proposed to predict the acceleration ratio. Ponder [11] and Nakamura and Kuroda [12] first independently gave a kinematic estimation to predict the enhanced settling velocity of suspension, i.e., the PNK theory. Acrivos and Herbolzheimer [13] then proposed an asymptotic analysis of sedimentation rate based on principles of continuum mechanics, which provided an interpretation of deviations between predictions of PNK theory and experimental observations by considering sediment thickness and resuspending mechanisms. These standard models, however, may not be sufficient or appropriate for describing the proppant settling process in inclined narrow channels [Fig. 1(b)].

First, previous models mainly consider suspension settling for small particle Reynolds numbers ( $Re_p \sim 1$ ), while sediment settling is ignored. As mentioned previously, proppant settling is constrained in a narrow channel. In this case, suspension settling can be accomplished very rapidly (within seconds) due to large particle Reynolds number ( $Re_p > 100$ ) and Grashof number [ $(H/W)^2 > 10^6$ ]. However, for a typical field-scale proppant transport process, the time scale can reach 1 h. Therefore, how fast sediment settles after suspension has deposited on the upward facing wall becomes the main concern.

Second, for the situations studied previously, the horizontal spreading length  $L$  is comparable to vessel width  $W$  and usually is much smaller than the container (tubes or vessels) height  $H$ , which is not the case for proppant transport where  $H \approx L \gg W$ . The difference of aspect ratio will influence the development of granular-induced instability. Herbolzheimer [14] reported that a Kelvin-Helmholtz analog instability can occur near the interface between clean fluid and suspension in the  $y$ - $z$  cross section during suspension settling in inclined vessels. Moreover, if the horizontal spreading length  $L$  is sufficiently large, the granular-induced instability can achieve further

development in the  $x$ - $z$  cross section. In Nevskii and Osipsov's work [15], a Rayleigh-Taylor analog instability is observed during the settling process of bandlike sediment in inclined domains through two-fluid model simulation. Above all, the related physical mechanisms within proppant settling in inclined narrow channels are more complex than those in previous works, which still need further investigation.

In this work, we aim to exploit the latent phenomena and mechanisms of the Boycott effect in proppant transport through numerical approaches. Generally, for most industrial-scale fluid-particle coupling systems, including proppant transport in petroleum engineering and catalyst fluidization reaction in chemical engineering, three characteristic scales exist [16,17]: microscale, mesoscale, and macroscale. For each scale, corresponding appropriate numerical approaches are available to investigate the characteristic behaviors. At the microscale, the particle surface's effects on the fluid field around particles are usually examined using direct numerical simulation (DNS) methods. In DNS methods, fluid field and particle-particle-wall, as well as fluid-particle interactions, are fully resolved, and basic drag laws can be derived for a small number of particles [18–20]. At the mesoscale, the unresolved computational fluid dynamics–discrete element method (CFD-DEM) method is usually employed to study particle-fluid interaction and spatial flow inhomogeneities (particle clustering) [21]. At the macroscale, how fluid field and averaged particle concentration field evolve, given submodels derived from smaller scales, is investigated using coarse-grid methods, such as the MultiPhase-Particle In Cell (MP-PIC) method [22,23], the two-fluid model [24], and the concentration transport model [25,26]. Generally, particle concentration distribution at the macroscale is important in engineering problems, and thus macroscale simulation methods are widely used in engineering designs. However, studying microscale and mesoscale behaviors of a particular particle conveying process is also crucial for developing high fidelity submodels.

In consideration of the advantages for capturing behaviors of granular-induced instabilities (particle clustering), in this work, the unresolved CFD-DEM method is utilized to elucidate proppant settling behaviors in inclined fractures. On the one hand, we intend to illustrate that the Boycott effect should not be ignored in the proppant transport process. On the other hand, we aim to build a modification model of proppant settling velocity that considers fracture inclination for macroscale simulations.

The remainder of this paper proceeds as follows. Section II presents the governing equations of fluid and particle phases, fluid-particle coupling force, and numerical issues. Section III illustrates two groups of validation tests, including Ergun's equation and sediment transport. In Sec. IV, problem settings for proppant settling in inclined fractures are described. Section V focuses mainly on the numerical results for various parametric studies, including fluid viscosity, proppant size, and density. Section VI provides the conclusion of this study.

## II. METHODOLOGY

### A. Fluid equation

In this work, fluid motion is governed by the volume-averaged incompressible Navier-Stokes equation [27,28]:

$$\frac{\partial}{\partial t}(\alpha_f) + \nabla \cdot (\alpha_f \bar{\mathbf{u}}_f) = 0, \quad (1)$$

$$\frac{\partial}{\partial t}(\alpha_f \bar{\mathbf{u}}_f) + \nabla \cdot (\alpha_f \bar{\mathbf{u}}_f \bar{\mathbf{u}}_f) = -\alpha_f \frac{1}{\rho_f} \nabla P_f + \alpha_f \nabla \cdot \bar{\boldsymbol{\tau}}_f + \alpha_f \bar{\mathbf{g}} + \bar{\mathbf{f}}_p, \quad (2)$$

where  $\alpha_f$  is the volume fraction of fluid;  $\bar{\mathbf{u}}_f$  is the mass-averaged fluid velocity;  $\rho_f$  and  $P_f$  are the fluid density and pressure, respectively;  $\bar{\boldsymbol{\tau}}_f = \nu_f(\nabla \bar{\mathbf{u}}_f + \nabla \bar{\mathbf{u}}_f^T)$  is the viscous stress tensor of fluid;  $\bar{\mathbf{g}}$  is the gravity acceleration; and  $\bar{\mathbf{f}}_p$  is the source term describing momentum transfer between the fluid phase and the particle phase.

According to [27], three different formulations exist for the governing equation of fluid, and the equation set II is adopted in this work. It is worth noting that, after substituting Eq. (1) into Eq. (2), an alternative form for the governing equation of fluid can be obtained as follows:

$$\frac{D\vec{u}_f}{Dt} = \frac{\partial\vec{u}_f}{\partial t} + \vec{u}_f \cdot \nabla\vec{u}_f = -\frac{1}{\rho_f}\nabla P_f + \nabla \cdot \tau_f + \vec{g} + \frac{1}{\alpha_f}\vec{f}_p, \quad (3)$$

which provides some intuition as to how the coupling of fluid and particle affects the original Navier-Stokes equation of pure fluid. It is obvious that the motion of a fluid element is determined by a combination of pressure gradient force, viscous force, gravity, and fluid-particle coupling force, respectively. Usually, Eqs. (1) and (2), known as conservative forms, are preferred for numerical discretization in practice.

In this work, turbulence is also considered by introducing the subgrid eddy viscosity  $\nu_t$ , and it is modeled following Vreman's [29] work, which offers several advantages over the original Smagorinsky's subgrid model.

## B. Particle equation

In this work, the discrete element method (DEM) [30] is utilized for modeling the particle phase. Particle motion is governed by Newton's second law and Euler's rotation equation [31,32]:

$$m_p \frac{d\vec{u}_p}{dt} = \vec{F}_f + \sum \vec{F}_c + \vec{F}_b, \quad (4)$$

$$\frac{d\vec{x}_p}{dt} = \vec{u}_p, \quad (5)$$

$$I_p \frac{d\vec{\omega}_p}{dt} = \vec{T}_c + \vec{T}_{rf}, \quad (6)$$

where  $m_p$ ,  $\vec{u}_p$ ,  $\vec{x}_p$ , and  $\vec{\omega}_p$  are the particle mass, velocity, displacement, and angular velocity, respectively;  $\vec{F}_f$  is the fluid-particle interaction force;  $\vec{F}_c$  is the collision force due to particle-particle and particle-wall interaction;  $\vec{F}_b$  is the body force, including gravity and driving force;  $I_p$  is the particle's moment of inertia; and  $\vec{T}_c$  and  $\vec{T}_{rf}$  are the collision torques due to collision force and rolling friction, respectively.

In this work, particle-particle and particle-wall interactions are described as coupling units of springs and dashpots, which is known as the soft sphere model [28]. For a contact pair of two particles, denoted as particles  $i$  and  $j$ , collision force exerted on particle  $i$  from particle  $j$  is calculated according to the following formulas [28]:

$$\vec{F}_{ij,n} = k_n \vec{\delta}_n + \gamma_n \vec{v}_n, \quad (7)$$

$$\vec{F}_{ij,t} = k_t \vec{\delta}_t + \gamma_t \vec{v}_t, \quad (8)$$

where subscripts  $n$  and  $t$  refer to the normal and tangential components, respectively;  $k_n$  and  $k_t$  are the normal and shear stiffness coefficients, respectively;  $\gamma_n$  and  $\gamma_t$  are the damping coefficients;  $\vec{\delta}_n$  is the overlap displacement between two particles;  $\vec{\delta}_t$  is the shear overlap between two particles, which is also known as the shear history; and  $\vec{v}_n$  and  $\vec{v}_t$  are the relative velocities of two particles.

In previous works, the Hertz contact model [33] is commonly adopted to calculate the stiffness coefficient, in which the spring is assumed to be nonlinear. In this work, for simplicity, the linear spring model is used, which permits a larger DEM time step to some extent. Moreover, shear stiffness is assumed to be the same as normal stiffness. Given a restitution coefficient  $e$ , the damping coefficient can be calculated as follows [23]:

$$\gamma_n = \frac{2\pi\sqrt{m_{\text{eff}}k_n}}{\sqrt{\pi^2 + \ln e}}, \quad (9)$$

where  $m_{\text{eff}} = \frac{m_i m_j}{m_i + m_j}$  is the effective mass of particle pair  $i$  and  $j$ .

Furthermore, the normal and tangential contact forces should fulfill Coulomb's friction law, which reads [34]

$$F_{c,t} \leq \mu F_{c,n}, \quad (10)$$

where  $\mu$  is the sliding friction coefficient.

In this work, rolling friction is also considered, and the rolling friction torque is calculated by [34]

$$\vec{T}_{rf} = -\mu_{rf} \|F_n\| R_i \vec{\omega}_{ij,t} / \|\vec{\omega}_{ij,t}\|, \quad (11)$$

where  $\mu_{rf}$  is the rolling friction coefficient;  $R_i$  is the radius of particle  $i$ ; and  $\vec{\omega}_{ij,t} = \vec{\omega}_{ij} - (\vec{\omega}_{ij} \cdot \vec{n}_{ij}) \vec{n}_{ij}$  is the projection of the relative angular velocity of particle  $i$  and  $j$  on the contact tangential plane.

### C. Fluid-particle coupling

According to Maxey and Riley's [35] pioneering work, the fluid-particle interaction force exerted on a particle can be modeled as a combination of drag force, pressure gradient force, viscous tensor gradient force, added mass force, Basset force, Saffman force, Magnus force, and other forces. In a gas-particle system, normally only pressure gradient force and drag force are considered as the dominant terms for gas-particle coupling. However, for dense fluid-particle flow simulation, such as sediment transport and proppant transport, viscous tensor gradient force, added mass force, and Saffman force can be significant, as pointed out by Sun and Xiao [32]. Therefore, in this work, we consider the above five terms for fluid-particle coupling.

First, Di Felice's drag model [36] is adopted to calculate the drag force according to the following formulas:

$$\vec{F}_{\text{drag}} = \frac{1}{2} \pi r^2 \rho_f C_d \|\vec{u}_f - \vec{u}_p\| (\vec{u}_f - \vec{u}_p), \quad (12)$$

$$C_d = \frac{24}{\text{Re}_p} \begin{cases} 8.33 \frac{\alpha_p}{\alpha_f} + 0.0972 \text{Re}_p & \text{if } \alpha_f < 0.8 \\ f_{\text{base}} \alpha_f^{-\zeta} & \text{otherwise} \end{cases}, \quad (13)$$

$$f_{\text{base}} = \begin{cases} 1 + 0.167 \text{Re}_p^{0.687} & \text{if } \text{Re}_p < 1000 \\ 0.0183 \text{Re}_p & \text{otherwise} \end{cases}, \quad (14)$$

$$\zeta = 3.7 - 0.65 \exp \left[ -\frac{1}{2} (1.5 - \log_{10} \text{Re}_p)^2 \right], \quad (15)$$

where  $C_d$  is the drag coefficient;  $r$  is the particle radius; and  $\text{Re}_p = \frac{2r \|\vec{u}_f - \vec{u}_p\|}{\nu_f}$  is the particle Reynolds number.

Second, Saffman lift force [37] is calculated by

$$\vec{F}_{\text{Saffman}} = 1.61 \rho_f D_p^2 \sqrt{\frac{\nu_f}{\|\vec{\omega}_f\|}} (\vec{u}_f - \vec{u}_p) \times \vec{\omega}_f, \quad (16)$$

where  $D_p$  is the particle diameter; and  $\vec{\omega}_f$  is the fluid vorticity.

Third, the added mass force [38] is modeled as follows:

$$\vec{F}_{\text{addmass}} = \frac{\rho_f V_p}{2} \left( \frac{D\vec{u}_f}{Dt} - \frac{d\vec{u}_p}{dt} \right), \quad (17)$$

where  $\rho_f$  is the fluid density,  $V_p$  is the particle volume, and  $\frac{D\vec{u}_f}{Dt}$  is the material derivative of the fluid.

Pressure gradient force  $\vec{F}_{\text{press}} = -V_p \nabla P_f$  and viscous tensor force  $\vec{F}_{\text{visc}} = \rho_f V_p (\nu_f \nabla \cdot \tau_f)$  are calculated from the fluid field. Then,  $\vec{F}_f$  in Eq. (4) can be written as

$$\vec{F}_f = \vec{F}_{\text{drag}} + \vec{F}_{\text{press}} + \vec{F}_{\text{visc}} + \vec{F}_{\text{Saffman}} + \vec{F}_{\text{addmass}}. \quad (18)$$

It is worth noting that the explicit pressure gradient force and viscous tensor force are due to the undisturbed flow, which can be considered as global effects at the large scale compared to the particle size. However, drag force is due to local effects, i.e., the *in situ* change of pressure and viscous tensor when one particle is placed in the fluid field [28,35]. In mesoscale simulations, the global effects are resolved, while the local effects are not because grid size is larger than particle size. Therefore, the drag force model is necessary for capturing the local effects.

Then,  $\vec{f}_p$  in Eq. (2) can be written in the following form according to the equation set II in Zhou's work [22]:

$$\vec{f}_p = \sum_i w_i (\vec{F}_{\text{drag},i} + \vec{F}_{\text{Saffman},i} + \vec{F}_{\text{addmass},i}), \quad (19)$$

where  $w_i$  is a weighting factor describing the contribution part from particle  $i$  to a certain fluid cell.

In fluid-particle two-phase flow, lubrication force is also an important mechanism. Due to the lubrication force, particle collisions immersed in fluid appear to be more inelastic compared to dry particle collisions. Usually, the lubrication force for two approaching particles can be derived based on the Stokesian dynamics, which relates to the particle size and fluid viscosity, as well as approaching velocity and distance [28,39,40]. For simplicity, the lubrication force is not directly considered in this work. Instead, we consider the lubrication effect by introducing a relatively small restitution coefficient, i.e.,  $e = 0.1$ , for particle-particle-wall collisions. This approximate approach is also adopted in previous works for studying sediment transport [31,32,41].

#### D. Numerical issues

In this work, fluid equations (1) and (2) are discretized in a three-dimensional (3D) Eulerian staggered grid with the finite volume method [42]. The convection term in Eq. (2) is discretized using the third-order QUICK scheme [43], and the pressure gradient and viscous terms are discretized using the second-order center difference scheme. For time discretization, a second-order scheme is adopted [42]. Fluid velocity and pressure are decoupled using the SIMPLE algorithm [44], and then the corresponding linear systems can be obtained for velocity components and pressure correction values. In this work, an open source package, i.e., PETSc [45], is adopted to efficiently solve these linear systems for every time step. The time step for the fluid solver is determined using the Courant number defined by  $\frac{\|\vec{u}_{\text{max}}\| \Delta t}{\Delta x}$ , which is set as less than 0.5 in this work.

Particle motion is solved within the Lagrangian framework, and Eqs. (4) and (5) are integrated using the velocity Verlet algorithm [46]. In the DEM method, most computational costs are due to the search of neighbor particles and collision force calculations. In this work, the linked-list searching algorithm [47] is utilized for fast neighbor search, with the  $O(N)$  order complexity. To calculate the fluid-particle interaction force exerted on particles, a trilinear interpolation function is adopted to estimate fluid quantities at the particle positions, such as fluid velocity, vorticity, and pressure gradient. It is worth noting that, in staggered Eulerian grids, control volumes for fluid velocity and pressure are not consistent, and therefore a total of four sets of interpolation operators are necessary for 3D problems [22]. The time step for DEM simulation is constrained by  $\frac{\pi}{5} \sqrt{\frac{m}{k_n}}$ , considering the numerical stability of linear springs [28].

In this work, parallelism strategies based on Message Passing Interface (MPI) are utilized to improve computational efficiency for various designed cases. Following [46], a three-way data transferring strategy is employed to transfer grid and particle data among various processors. Within the current framework, a large-scale case with 1 000 000 particles can be accomplished within 1 day at a 32-core occupied workstation.

Figure 2 illustrates the flowchart of the code implementation of this work. Governing equations of fluid phase and particle phase are sequentially solved with explicit interphase coupling. Prior to solving fluid governing equations, particle volume fraction and momentum source due to fluid-particle coupling need to be updated based on particle displacements and hydrodynamic forces.

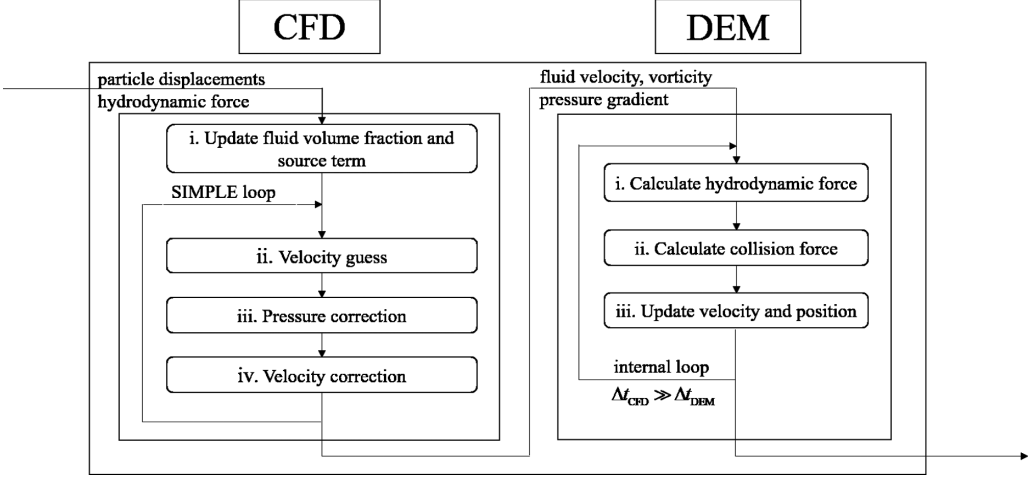


FIG. 2. Flowchart of the unresolved CFD-DEM framework.

When solving particle equations, fluid fields, including velocity, vorticity, and pressure gradient, are utilized for calculating hydrodynamic forces, including drag force, Saffman force, and pressure gradient force. As usual, the DEM time step is much smaller than that of the CFD time step, and thus an internal loop is required in the DEM module to keep the fluid and particle phase advancing at the same time level.

### III. VALIDATION TESTS

#### A. Ergun equation

The Ergun equation [48] describes the relationship between pressure drop and averaged bulk velocity for the flow in granular medium as follows:

$$\frac{\Delta P}{L} = \frac{150\mu_f (1 - \alpha_f)^2}{d_p^2 \alpha_f^3} U + \frac{1.75\rho_f (1 - \alpha_f)}{d_p \alpha_f^3} U^2, \quad (20)$$

where  $\Delta P$  is the pressure drop,  $L$  is the length of granular medium in the flow direction, and  $U = \alpha_f u_f$  is the averaged bulk velocity.

Simulation parameters of this test are listed in Table I. First, pure DEM simulation is performed to obtain an arbitrary arrangement of the granular medium, of which the averaged volume fraction of fluid is estimated as 34%. Various driving forces are then exerted on the right-hand side of Eq. (2), with all six boundary sides set as periodic. After several time steps, the fluid field reaches a steady

TABLE I. Parameter settings for the Ergun equation test.

Parameter	Value	Parameter	Value
Fluid density	1000 kg/m <sup>3</sup>	Particle density	2650 kg/m <sup>3</sup>
Fluid viscosity	1 cp	Particle diameter	1 mm
Domain size	0.02 × 0.02 × 0.04 m <sup>3</sup>	Mesh size	10 × 10 × 20
Stiffness coefficient	3.5 N/m	Restitution coefficient	0.1
Friction coefficient	0.6	Rolling friction coefficient	0.1
Particle numbers	19561	Porosity	0.36

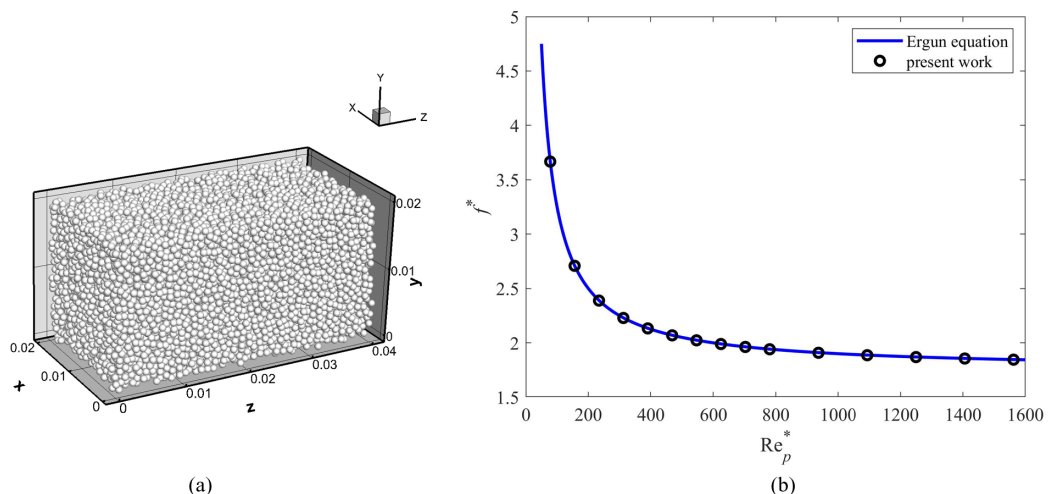


FIG. 3. Illustration of particle-packed porous medium (a) and comparison results of friction factor  $f^*$  versus modified particle Reynolds number  $Re_p^*$  between the Ergun equation and the present work (b).

state, and the averaged bulk velocity is estimated. Figure 3 plots the dimensionless friction factor  $f^*$  of the packed bed against the modified particle Reynolds number  $Re_p^*$ , defined as follows:

$$f^* = \frac{\Delta P}{L} \frac{d_p}{\rho_f U^2} \frac{\alpha_f^3}{1 - \alpha_f} = \frac{150}{Re_p^*} + 1.75, \quad (21)$$

$$Re_p^* = \frac{\rho_f d_p U}{\mu_f (1 - \alpha_f)}. \quad (22)$$

Numerical results show good agreement with the analytical solution, and the relative errors of all cases are less than 0.5%. By this test, the calculations of the drag forces on particles and the source terms fed back to the fluid momentum equation are validated.

## B. Sediment transport

In this part, a dynamic test is performed by simulating the sediment transport process [31]. Simulation parameters are listed in Table II. Simulation is performed in a 3D cuboid box. The flow direction is the  $+z$  direction, and the gravity direction is the  $-y$  direction. Four boundaries of  $x$  and

TABLE II. Parameter settings for sediment transport.

Parameter	Value	Parameter	Value
Fluid density	1000 kg/m <sup>3</sup>	Particle density	2650 kg/m <sup>3</sup>
Fluid viscosity	1 cp	Particle diameter	0.5 mm
Domain size	0.06 × 0.04 × 0.12 m <sup>3</sup>	Mesh size	60 × 40 × 120
Stiffness coefficient	3.5 N/m	Restitution coefficient	0.1
Friction coefficient	0.6	Rolling friction coefficient	0.1
Particle numbers	288000	Simulation time	10 s
CFD time step	0.5 ms	DEM time step	10 μs
$z$ -Direction averaged bulk velocity $\langle\langle w \rangle\rangle$	0.6–1.2 m/s		



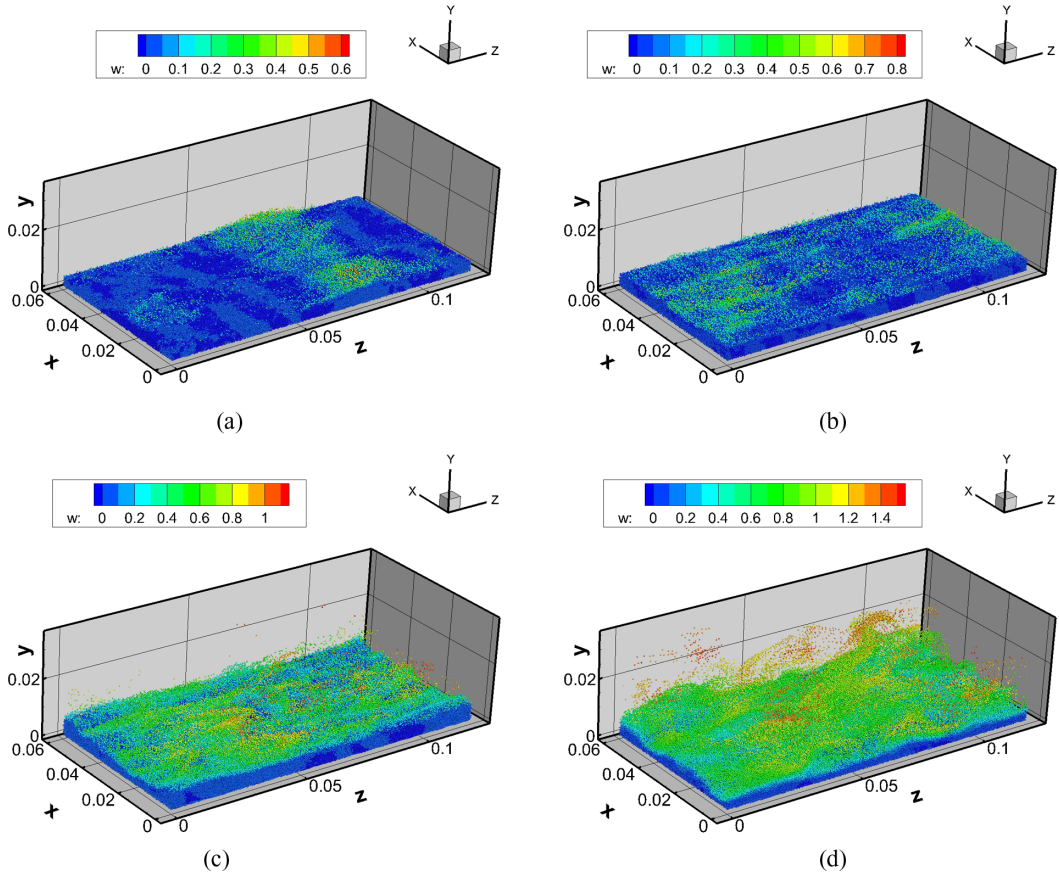


FIG. 4. Images of sediment transport of four cases. (a), (b): bed-load regime; (c), (d): suspended-load regime. The direction of gravity is  $-y$ , and the downstream direction is  $+z$ .

$z$  directions are set as periodic. The  $-y$  direction is a nonslip wall boundary, and the  $+y$  direction is set as a slip mirror condition. An additional driving force is appended in the fluid momentum equation to assure an expected averaged bulk velocity for each time step. Sediment transport is a two-phase fluid-particle coupling problem similar to the proppant transport. However, compared to the proppant settling as illustrated in Fig. 1(b), channel width in this test is much larger than the fracture width in the  $y$  direction.

Initially, the channel is exactly located in a horizontal status without inclination, and particles are all closely packed in the bottom of the channel. As net bulk velocity increases, particles lying on the surface of the packed particle bed start creeping under the shear stress and drag force, which corresponds to the “bed-loaded” regime. As bulk velocity experiences a further increase, an increasing number of particles start to suspend into the main flow region and the flow pattern appears to be chaotic, which corresponds to the “suspended-load” regime. In the suspended-load regime, all the fluid-particle coupling forces mentioned in Sec. II C play important roles in the sediment transport.

Figure 3 presents images of particle distributions for four cases, i.e., time-averaged bulk velocity  $\langle\langle w \rangle\rangle = 0.6, 0.8, 1.0,$  and  $1.2$  m/s, respectively. It is clear that, for the first two cases, the flow regime is bed-load dominated, while the suspended-load regime dominates in the latter two cases.

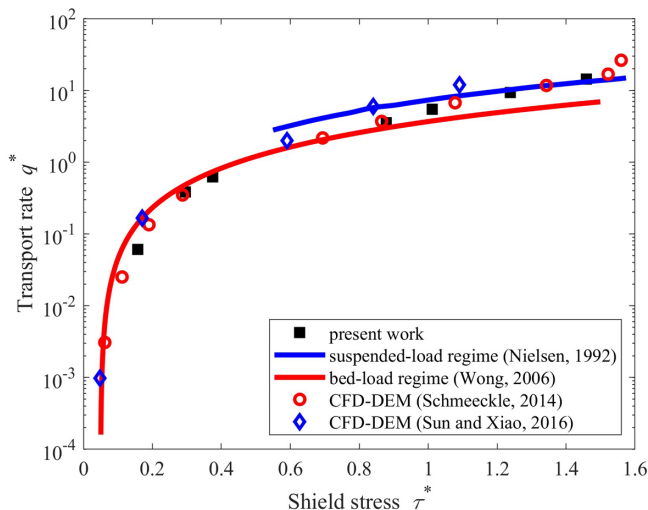


FIG. 5. Nondimensional transport rate versus shield stress in sediment transport tests. The red solid line is Wong and Parker's [49] empirical curve describing the bed-load regime, and the blue solid line is Nielsen's [50] empirical curve describing the suspended-load regime. The black square dots indicate numerical results of the present work, and the red circle and blue diamond are the numerical results of CFD-DEM methods in previous studies [31,32].

To quantitatively compare the results with previous works in the literature, we show the curves (cf. Fig. 4) of dimensionless transport rate  $q^*$  against shield stress  $\tau^*$ :

$$q^* \equiv \sum_i V_p u_{p,z} / A \left[ \left( \frac{\rho_p}{\rho_f} - 1 \right) g d_p^3 \right]^{1/2}, \quad (23)$$

$$\tau^* = \rho_p H \bar{f} / [\rho_f (\rho_p - \rho_f) g d_p], \quad (24)$$

where  $V_p$  and  $u_{p,z}$  are the particle volume and downstream velocity of the particle, respectively;  $A$  is the horizontal plane area;  $H$  is the domain height; and  $\bar{f}$  is the time-averaged driving force.

Figure 5 shows that the simulation results are in close accordance with those in the extant literature. Cases of  $\langle w \rangle = 0.6, 0.7, \text{ and } 0.8$  m/s are bed-load regime dominated, and cases of  $\langle w \rangle = 0.9, 1.0, 1.1, \text{ and } 1.2$  m/s are suspended-load regime dominated.

#### IV. PROBLEM DESCRIPTION

Figure 6 presents a typical proppant transport process in hydraulic fracturing. In this case, a vertical well is completed, and fracturing fluid with proppant is pumped into the stimulated fracture through perforations. The horizontal direction represents the main direction for fracture propagating. Then, the proppant settles and forms a sand bed at the bottom of the fracture. For industrial-scale proppant transport, it is challenging to resolve full-scale details through simulation because of the large scalar ratio. Generally, the fracture length can reach hundreds of meters, while the proppant size is less than a millimeter. Consequently, a macroscale equation is usually utilized to describe large-scale behaviors, in which volume-averaged approaches are adopted and additional models are introduced to capture the unresolved physical mechanisms, including particle settling and packing at smaller scales. In this work, we are primarily concerned with mesoscale particle settling behaviors in inclined fractures, and the modified settling models can be extracted from simulation results.

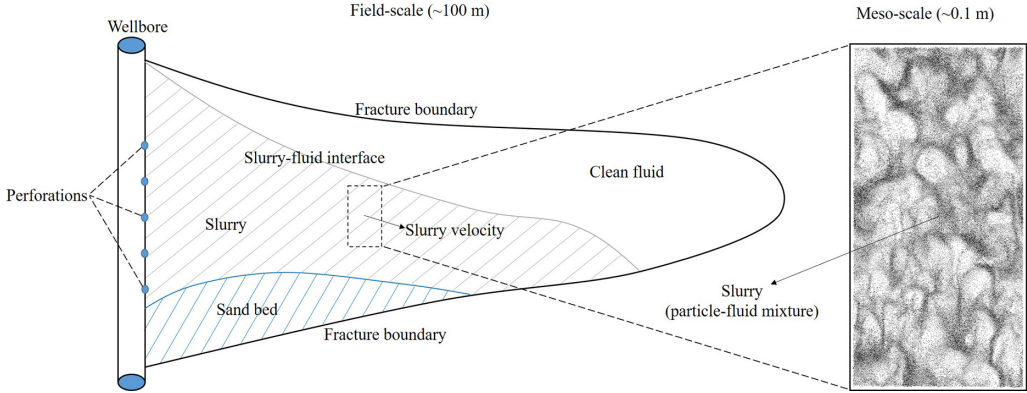


FIG. 6. Illustration of the relationship between field-scale (left) and mesoscale (right) study for proppant transport. The blue shaded region indicates the packed sand bed, and the gray shaded region indicates the suspended slurry.

Then, by utilizing the modified models in large-scale simulation, the eventual spatial distributions of slurry and sand bed are obtained.

It should be noted that, in inclined fractures, even though the proppant quickly deposits and temporarily forms a sediment layer on the upward facing wall of the fracture, the sediment will continue settling and evolving in cases of high inclination angles. Then, from the perspective of volume average, as long as the proppant keeps settling and does not form a close-packed sand bed in the bottom of the fracture, the ensemble of fluid-particle mixture can still be considered as slurry, regardless of the embedded complex dynamic behaviors.

In this work, the domain of focus is illustrated as the zoomed-in dashed window shown in Fig. 6. The domain size is approximately several decimeters in this case, and then mesoscale behaviors can be precisely determined using the unresolved CFD-DEM method. At the large scale, slurry velocity can also fluctuate with space and time. Here it is assumed that the large-scale slurry velocity does not affect mesoscale behaviors. Moreover, slurry velocity is set to be zero in later studies, which can be regarded as a baseline.

The simulation domain is illustrated Fig. 1(b). The  $-z$  direction is the settling direction. In the  $y$  direction, both sides are set as the nonslip boundary condition for the fluid phase and the solid wall condition for the particle phase. The other four sides in the  $x$  and  $z$  directions are set as periodic for both the fluid and particle phases. The inclination angle  $\theta$  is defined as the intersection angle between the gravity direction and the  $x$ - $y$  plane, and then fractures of  $\theta = 0$  and  $\theta = \frac{\pi}{2}$  indicate rigorously horizontal and vertical fractures, respectively.

In this work, the periodic boundary condition is applied in the settling direction, and an additional driving force is adopted to achieve zero slurry velocity every time step in the settling direction as follows:

$$\langle w_s \rangle \equiv \alpha_f \langle w_f \rangle + \alpha_p \langle w_p \rangle = 0, \quad (25)$$

where  $\langle w_s \rangle$  is defined as the slurry velocity, or averaged bulk velocity; and  $\langle w_f \rangle$  and  $\langle w_p \rangle$  are phase-averaged velocity components in the settling direction of the fluid phase and the particle phase, respectively.

If the simulation domain is too small, however, the statistical averaged settling velocity will diverge from the actual results. Therefore, in consideration of the balance of computational cost and statistical accuracy, the domain size is set to be sufficiently large to capture mesoscale behaviors. For an eight-core occupied workstation, the execution time of a single case is within 1 h. Simulation parameters for the base case are listed in Table III. Properties of the fluid and particles are designed based on engineering parameters of proppant transport.

TABLE III. Parameter settings for proppant settling in inclined fractures (base case).

Parameter	Value	Parameter	Value
Fluid density	1000 kg/m <sup>3</sup>	Particle density	2650 kg/m <sup>3</sup>
Fluid viscosity	1 cp	Particle diameter	0.6 mm
Domain size	0.2 × 0.1 × 0.006 m <sup>3</sup>	Mesh size	200 × 100 × 6
Stiffness coefficient	3.5 N/m	Restitution coefficient	0.1
Friction coefficient	0.6	Rolling friction coefficient	0.1
Particle numbers	120000	Simulation time	20 s
CFD time step	1 ms	DEM time step	20 μs
Inclination angles	15°–90° (interval: 5°)		

Through dimensional analysis, the following dimensionless numbers are obtained for the above transport process:

$$\text{Ga} = \frac{\sqrt{gW^3}}{\nu_f}, \quad \text{Sg} = \frac{\rho_p}{\rho_f}, \quad \text{Sr} = \frac{D}{W}, \quad (26)$$

where Ga is the Galileo number, Sg is the density ratio, and Sr is the size ratio of particle diameter over fracture width.

Combined with other dimensionless variables, including inclination angle  $\theta$ , averaged volume fraction of fluid  $\alpha_f$ , and friction coefficients, the acceleration ratio of interest in this work can be expressed as

$$r_{\text{acc}} = \frac{\bar{w}}{\bar{w}_{\theta=\pi/2}} = f(\text{Ga}, \text{Sg}, \text{Sr}, \theta, \alpha_f, \dots) \quad (27)$$

In this work, collision parameters for DEM are assumed to be constant for simplicity, and in a later section, various curves describing the relationship between  $r_{\text{acc}}$  and  $\theta$  are obtained under several conditions through numerical results.

## V. RESULTS AND DISCUSSIONS

### A. Elementary settling process and mechanisms

First, the case of the inclination angle  $\theta = 75^\circ$  is taken as an example to provide insight into the proppant settling process in an inclined fracture. Figure 7 presents ten images at different times during the settling process. It is clear that the proppant is uniformly distributed at the early stage [Figs. 7(a)–7(c)]. Plume structures then gradually form [Figs. 7(d)–7(g)], and strong spatial inhomogeneity with spike structures (particle clustering) is finally observed in the  $x$ - $z$  plane [Figs. 7(h)–7(j)].

Figure 8 illustrates the time-varying curve of phase-averaged settling velocity, defined as

$$\langle w_p \rangle \equiv \frac{1}{N_p} \sum_{i=1}^{N_p} w_{p,i}, \quad (28)$$

where  $N_p$  is the total particle number in the simulation domain, and  $w_{p,i}$  is the  $z$ -direction velocity component of particle  $i$ .

According to the curve trend illustrated in Fig. 8, and combined with the numerical results shown in Fig. 7, the particle settling process in inclined narrow channels can be roughly divided into three stages: stratified acceleration stage (stage I), resuspended stage (stage II), and secondary instability stage (stage III). Figure 9 provides a brief illustration of these stages to show the underlying mechanisms.

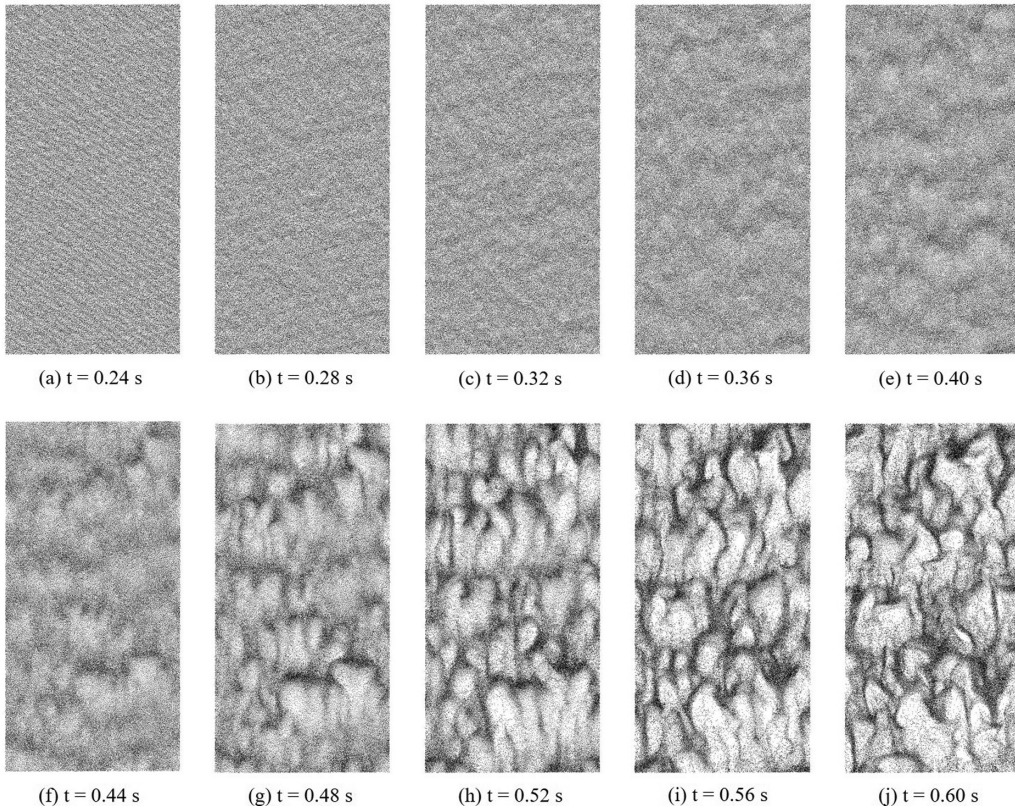


FIG. 7. Images of proppant settling in an inclined fracture of the case  $\theta = 75^\circ$  (plotted on the  $x$ - $z$  plane). Proppant particles are scattered as black points.

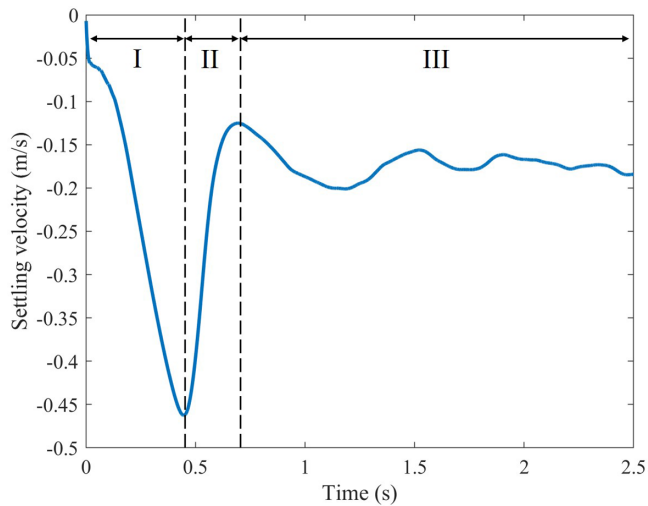


FIG. 8. Phase-averaged settling velocity curve in an inclined fracture of the case  $\theta = 75^\circ$ . The curve can be divided into three stages over time: stratified acceleration stage (stage I); resuspended stage (stage II); and secondary instability stage (stage III).

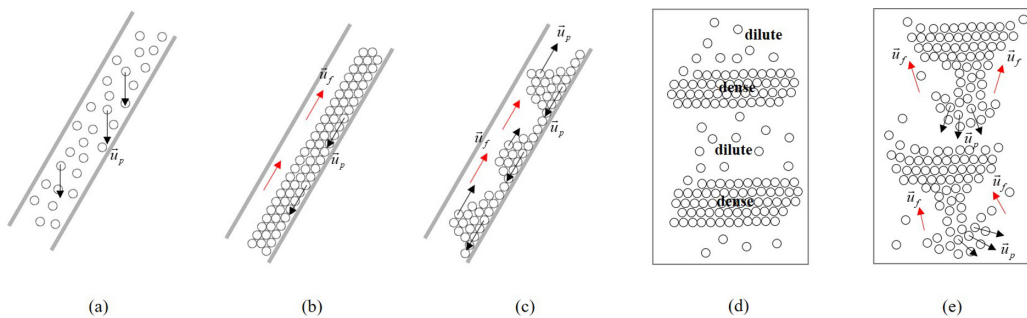


FIG. 9. Different stages of development for granular-induced instability. (a), (b) stratified acceleration stage (I); (c), (d) resuspended stage (II); (e) secondary instability stage (III). (a)–(c) are presented on the  $y$ - $z$  plane, and (d), (e) are presented on the  $x$ - $z$  plane. Red and black arrows indicate velocity vectors of the fluid phase and the particle phase, respectively.

(I) Stage I: Stratified acceleration. Initially, proppant is suspended uniformly in the channel, as shown in Fig. 9(a). Proppant suspension then quickly settles on the bottom side of the channel under gravity. The settling process forms stratified layers where the particle phase lies on the bottom layer, and the pure fluid phase lies on the upper layer. Subsequently, driven by the gravity component in the settling direction, particles and fluid keep accelerating in opposite directions [Fig. 9(b)], and shear stress continues to increase. During this stage, the phase-averaged settling velocity keeps increasing under the convection effect, as shown in Fig. 8.

(II) Stage II: Resuspended. Under a strong shear effect, granular-induced interface instability occurs, which is analogous to Kelvin-Helmholtz instability, in which the heavy layer is covered by the lighter layer, and is under the transverse shear effect. Then, interfaces gradually deform, and plume structures (KH modes) begin to develop, as shown in Figs. 7(e) and 7(f). Unlike most KH instability cases, however, a miscible mixing process in granular-laden flow does not exist. Therefore, after interface deformation, particle distribution becomes uneven, and this unevenness continues to increase, as indicated in Fig. 9(c), and particles on the bottom layer start to resuspend to the upper layer. This mechanism assists in propelling momentum exchange between the upper and lower layers. Consequently, the phase-averaged settling velocity keeps decreasing, and the curve continues to rise during this stage, as shown in Fig. 8. It is worth noting that the resuspended mechanism in this stage is similar to that of sediment transport discussed in Sec. III B. There exists a critical shear velocity for the change from the bed-load regime to the suspended-load regime in sediment transport. In this case, the stratified acceleration stage (stage I) is necessary to obtain a sufficient shear velocity to induce the subsequent KH instability.

It is worth noting that Herbolzheimer [14] also reported another granular-induced KH instability, which occurs near the interface between clarified fluid and suspension. Compared to the aforementioned KH instability in this work, which occurs near the clarified fluid–sediment interface, the induced mechanism is similar. Qualitatively, both of them are caused by shear effects near interfaces (between pure fluid and suspension or sediment) and can be classified into Kelvin-Helmholtz instability. On the other hand, the differences between these two types of instabilities are also readily apparent. Suspension of low concentration can still be considered as a continuum similar to a Newtonian fluid. Under reasonable assumptions, the developing rate can be estimated through theoretical analysis, as done by Herbolzheimer [14]. However, the constitutive laws of mixture of sediment and fluid in this work are more complex.

(III) Stage III: Secondary instability. From the configuration illustrated in Fig. 9(c) on the  $x$ - $z$  plane [Fig. 9(d)], one can discern that this situation leads to another instability, i.e., the Rayleigh-Taylor instability. At the end of the resuspended stage, dense and dilute regions become separated on the  $x$ - $z$  plane, and interfaces begin to form where the heavy phase (dense) lies on the upper

side of the light phase (diluted). Subsequently, another granular-induced instability, analogous to Rayleigh-Taylor instability, occurs driven by the gravity component in the settling direction. As a result, spike structures (RT modes) start to form and evolve, as shown in Figs. 7(h)–7(j) and 9(e). Due to the secondary instability, a trend of reacceleration can be observed at the start of stage III in Fig. 8. Finally, the fluid-particle system becomes fully developed and achieves a pseudo steady state, with the phase-averaged settling velocity reaching a plateau, irrespective of statistical fluctuations, as indicated in Fig. 8.

### B. Correlation curves

The relationship between ensemble-averaged settling velocity and the inclination angle is also a primary concern in this work. In this part, 16 cases with various inclination angles ( $\theta = 15^\circ, 20^\circ, 25^\circ, \dots, 85^\circ, 90^\circ$ ) are designed. The ensemble-averaged settling velocity is defined as follows:

$$\langle\langle w_p \rangle\rangle \equiv \frac{1}{N_t N_p} \sum_{n=1}^{N_t} \sum_{i=1}^{N_p} w_{p,i}^n, \quad (29)$$

where  $N_t$  denotes the total time steps of the time interval of interest. For this study, the averaged settling velocity during the pseudo-steady stage (stage III) becomes the main focus because it represents the long-term settling behavior of the particle phase. Most importantly, the ensemble-averaged settling velocity can be regarded as the time-averaged result of the phase-averaged particle velocity. The averaged time interval ranges from 5 to 20 s, in which the particle-fluid system is fully developed.

Figure 10 shows images of eight cases at the end of the simulation time. For cases of  $\theta = 40^\circ$ – $80^\circ$ , strong spatial heterogeneities of particle distributions are observed, implying that the particle cloud evolution experienced the aforementioned three stages in these cases. Moreover, as the inclination angle increases, the scale length of spike structures decreases due to the increase of the gravity component in the settling direction. For cases of  $\theta < 35^\circ$ , bed-load regimes are recognized because the development of the stratified acceleration stage (stage I) is poor, and the shear velocity is not sufficient to induce KH instability. For the case of  $\theta = 90^\circ$ , because the gravity component in the width direction is zero, the particle cloud keeps suspending during the entire settling process. However, as the particle cloud evolves, local heterogeneities of particle volume fraction gradually form, and small-scale spikes can also be observed in Fig. 10(h).

Figure 11 shows the corresponding correlation curve. It is clear that a peak value of  $\langle\langle w_p \rangle\rangle = -0.1816$  m/s exists at the inclination angle  $\theta = 65^\circ$ . Compared to the vertical case, in which  $\langle\langle w_p \rangle\rangle = -0.0802$  m/s, the acceleration ratio reaches approximately 2.25. Combined with the images presented in Fig. 10, the correlation curve can be roughly divided into four parts as follows:

(I)  $\theta \leq 15^\circ$ . In these cases, the gravity component in the settling direction is not sufficiently large to drive the fluid-particle mixture. Consequently, particles settle on the bottom side of the channel, reaching a self-supporting state, and the statistically averaged settling velocity is zero. Particle-particle–wall damping mechanisms, including friction force and rolling friction, dominate the process in these cases.

(II)  $15^\circ < \theta \leq 35^\circ$ . As the gravity component in the settling direction increases, the particle-packed bed begins to move. The fluid-particle mixture starts to enter stage I, i.e., the stratified acceleration stage. Therefore, a steep decline is observed in the correlation curve in this interval of inclination angles. In these cases, the stratified acceleration mechanism in the  $y$ - $z$  plane dominates the settling process.

(III)  $35^\circ < \theta \leq 65^\circ$ . As the gravity component further increases, the shear velocity reaches a critical value to induce KH instability, and the fluid-particle mixture starts to enter stage II and stage III. Although a temporary decline of averaged settling velocity exists, as shown in Fig. 8, there is a

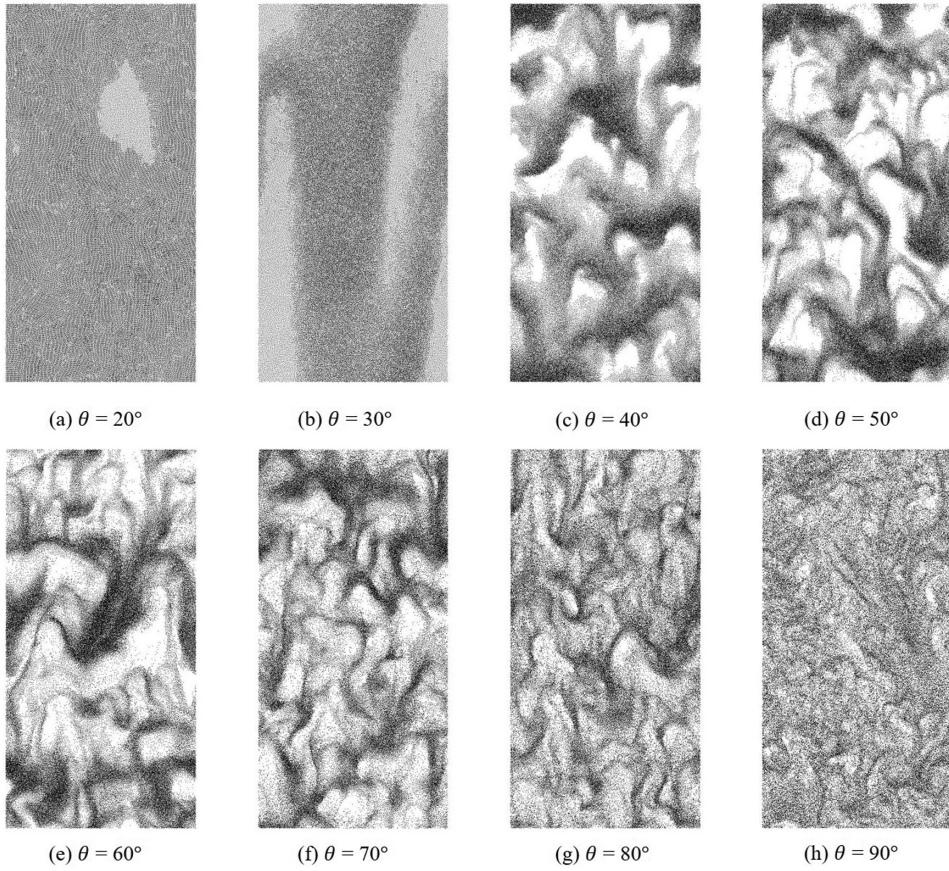


FIG. 10. Images of proppant settling in inclined fractures of various inclination angles (base case).

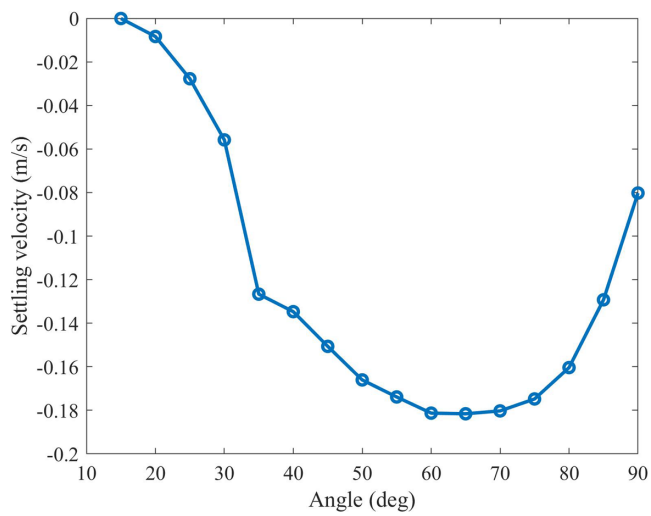


FIG. 11. Correlation curve between ensemble-averaged settling velocities and inclination angles.



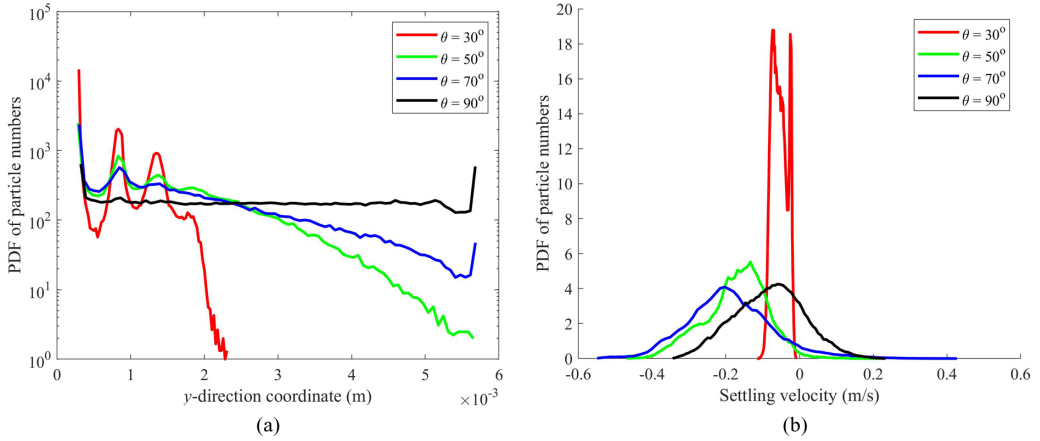


FIG. 12. Particle distributions of y-direction coordinates (a) and settling velocity (b).

further acceleration of settling velocity due to the secondary RT instability. Both fluid-particle and particle-particle-wall interactions play significant roles in these cases.

(IV)  $65^\circ < \theta \leq 90^\circ$ . The averaged settling velocity reaches a peak value near  $\theta = 65^\circ$ . As the inclination angle further increases, the stratified acceleration effect becomes weaker because of the decreasing gravity component. The increasing inclination angle leads to a stronger particle resuspension, and the particle distribution inclines to be more uniform in the width direction. As a result, the absolute ensemble-averaged settling velocity begins to decrease monotonically.

Here, the probability density functions of the particles' y-direction coordinate and settling velocity are also obtained to understand how the inclination angles affect the proppant settling process, shown in Fig. 12.

For the case of  $\theta = 90^\circ$ , particles are basically uniformly distributed over the width direction, with sudden rises near the two solid boundaries. The boundary rises indicate that particle-wall interactions are significant in this process, even though there are no additional forces driving particles in the width direction. Moreover, the central plateau in the case of  $\theta = 90^\circ$  can be considered as a baseline for particle suspending magnitude. As shown in Fig. 12(a), as the inclination angle  $\theta$  decreases, the high-value tail also declines, implying that particle resuspension is gradually suppressed by the increasing gravity component in the width direction. It is clear that, for low-value tails, multi-modal distributions are observed for cases of  $\theta = 30^\circ$ ,  $50^\circ$ , and  $70^\circ$ . This is because proppant particles are packed into several layers near the wall boundary due to the gravity component in the  $-y$  direction. Under this configuration, preferential locations for particles exist. For example,  $y = 0.3$  mm indicates the first layer of particles. This effect is particularly evident in cases with low inclination angles. However, as the inclination angle increases, this effect is gradually diminished due to the particle resuspension mechanism. As shown in Fig. 12(b), for cases of  $\theta = 50^\circ$ ,  $70^\circ$ , and  $90^\circ$ , the distribution of the particle settling velocity spreads widely around the mean value and appears to be a single-modal type. In contrast, for the case of  $\theta = 30^\circ$ , a bimodal distribution is observed due to the multilayer configuration.

### C. Effects of parameters

In practical engineering designs, several approaches are effective in preventing the rapid settling of proppant, such as increasing fracturing fluid viscosity and utilizing proppant with small size and density. In this part, another three groups of cases are designed to investigate whether these approaches remain effective for proppant settling in inclined fractures.

In the base case, three dimensionless numbers listed in Eq. (26) are  $Ga = 1456$ ,  $Sr = 0.1$ , and  $Sg = 2.65$ . We then increase fluid viscosity from 1 to 10 cp, and decrease proppant size from 0.6 to 0.4 mm. In addition, proppant density is changed from 2650 to 1500 kg/m<sup>3</sup>. Therefore, the dimensionless numbers are changed to  $Ga = 145.6$ ,  $Sr = 0.0667$ , and  $Sg = 1.5$ , for additional groups of cases. For each group, 16 cases with various inclination angles  $\theta = 15^\circ - 90^\circ$  are designed to obtain correlation curves, similar to the base case.

Particle distributions of the three groups of cases at the end of the simulation are given in Fig. 13. Similar to the base case, particles are uniformly distributed for cases of low inclination angles. In cases of moderate inclination angles, particle clustering behaviors can be observed due to secondary instability.

Compared to the base case, the high viscosity group [Figs. 13(a)–13(d)] has a much larger scale length of spike structures because of the suppression of the development of small RT modes. Due to the viscous mechanism, particle distribution in the case of  $\theta = 90^\circ$  is also more uniform than that of the base case. For the group with small particle size, to ensure the same total particle volume fraction, 405 000 particles are simulated in these cases. Therefore, the rendered results appear to be darker than other cases, as shown in Figs. 13(e)–13(h). Because the particles' Stokes number is smaller than that of the base case, the particles' tracing capability is stronger. Consequently, granular-induced instability is more likely to occur in cases of small inclination angles, as shown in Fig. 13(e). For the group with small particle density, settling behaviors are similar to the base case for  $\theta < 70^\circ$ . In the case of  $\theta = 90^\circ$ , particle distribution is more uniform because the lower density difference between fluid and particle helps to prevent local granular-induced instability.

Figure 14 provides a quantitative comparison of the correlation curves of the four groups, including the base case. From Fig. 14(a), it can be seen that, in rigorous vertical fractures ( $\theta = 90^\circ$ ), the absolute ensemble-averaged settling velocities of the cases designed in this part are all smaller than that of the base case. The situation, however, becomes complex as the inclination angle varies. As discussed in Sec. V A, the acceleration of particle settling in inclined narrow channels is attributed to the balance of three mechanisms, i.e., stratified acceleration, particle resuspension, and secondary instability mechanisms. Particularly, the second one is attributable to deceleration, while the other two are due to acceleration. Combined with the above inferences, the effects of parameters can be summarized as follows:

(I) High-viscosity group  $Ga = 145.6$ . For high-viscosity cases, stratified acceleration, particle resuspension, and second instability effects are all suppressed to some extent. As a result, compared to the base case, the absolute ensemble-averaged settling velocity decreases. However, the quiescent settling velocity of this group is too small, and the acceleration ratio reaches a peak value of approximately 6. Furthermore, due to the viscous effect, granular-induced instability is more difficult to develop. As a consequence, a higher inclination angle is required for particle resuspension, and the peak value shifts from  $\theta = 65^\circ$  to  $\theta = 75^\circ$  compared to the base case.

(II) Low particle size group  $Sr = 0.0667$ . First, decreasing particle size has no significant effects on the stratified acceleration mechanism. Second, as the particle size decreases, the particles' Stokes number is smaller, and particle resuspension is more likely to occur. Third, better tracing capability assists the development of secondary instability. Overall, the peak value of the absolute settling velocity curve is slightly larger than the base case, implying the dominance of the third effect over the second effect. Decreasing particle size does not reduce the absolute settling velocity in inclined fractures in most cases.

(III) Low particle density group  $Sg = 1.5$ . From Fig. 14(a), it can be seen that the lower particle density group achieves comparatively better performance. In fact, decreasing the particles' density leads to a weaker stratified acceleration effect, a stronger resuspended effect, and a diminished secondary instability effect. Both acceleration mechanisms, i.e., stage I and stage III, are suppressed, and the deceleration mechanism, i.e., stage II, is strengthened. Therefore, compared to the base case, the peak value of the absolute settling velocity decreases from 0.1816 to 0.109 m/s. However, even in this case, the acceleration ratio reaches approximately 3, as shown in Fig. 14(b), implying that the Boycott effect cannot be ignored.

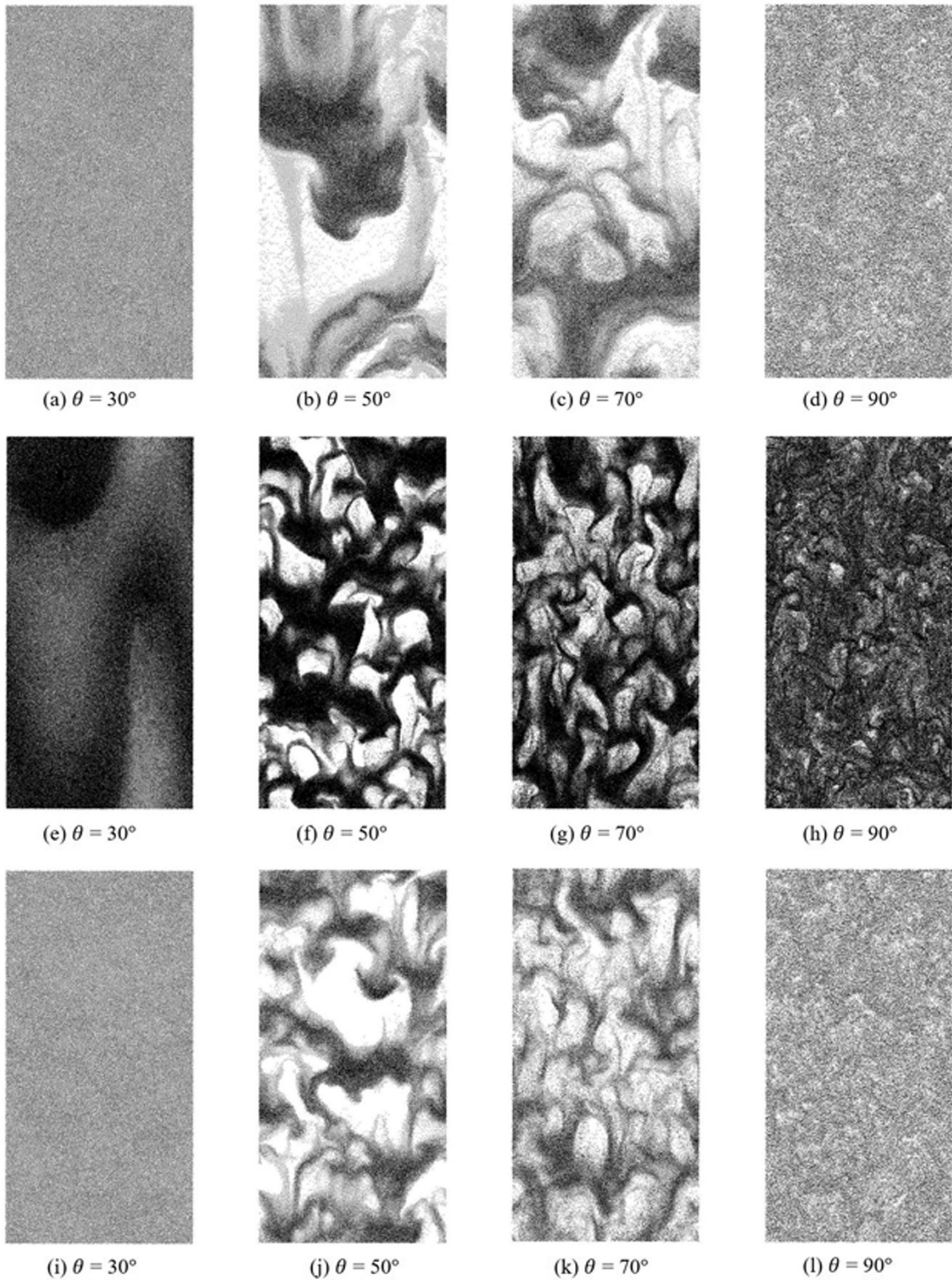


FIG. 13. Images of proppant settling in inclined fractures of various inclination angles: (a)–(d) for cases  $Ga = 145.6$ ; (e)–(h) for cases  $Sr = 0.0667$ ; (i)–(l) for cases  $Sg = 1.5$ .

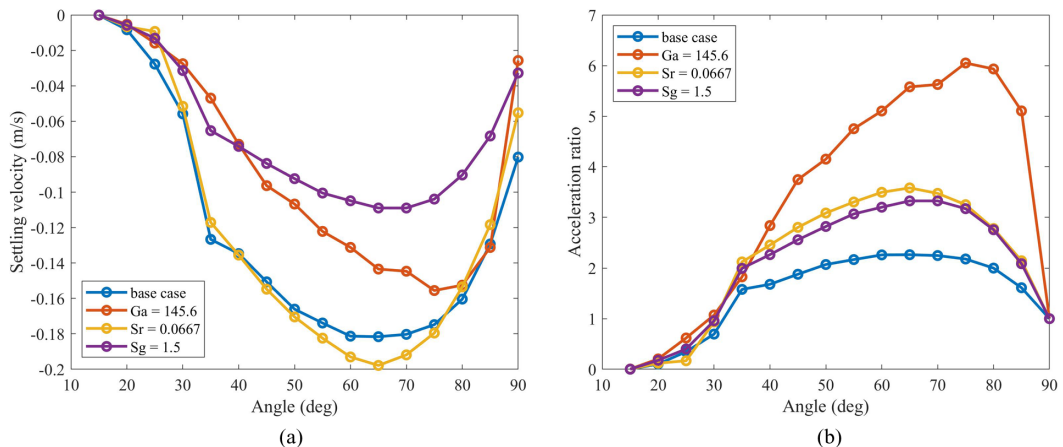


FIG. 14. Curves of ensemble-averaged settling velocity (a) and acceleration ratio (b) against inclination angles for four groups of cases. For the base case, the dimensionless numbers are  $Ga = 1456$ ,  $Sr = 0.1$ , and  $Sg = 2.65$ .

## VI. CONCLUSIONS

In this work, the unresolved CFD-DEM method is utilized for investigating proppant settling in inclined fractures. In order to validate our in-house codes, a static test of the Ergun equation, and a dynamic test of sediment transport, are performed under various conditions. The problem of the proppant settling process in inclined fractures is then proposed and formulated. Various groups of cases are designed to elucidate the process. Embedded physical mechanisms are comprehensively discussed to provide deeper insights, and quantitative correlation curves are obtained for various conditions. In summary, the following conclusions can be drawn:

(I) Settling acceleration of proppant in inclined fractures is attributed to the balance of three mechanisms, i.e., stratified accelerating, resuspension, and secondary instability mechanisms. Each mechanism corresponds to a particular stage during settling.

(II) Particle clustering behaviors are found during the settling process in inclined channels, which are induced by a strong shear effect during the resuspension stage and developed during the secondary instability stage. The former mechanism is analogous to Kelvin-Helmholtz instability, and the latter one is analogous to Rayleigh-Taylor instability.

(III) As inclination angle varies, a peak value exists in the correlation curves for describing the acceleration ratio, ranging from 2 to 6 in this work. As fluid viscosity increases, the inclination angle of the peak value shifts to a higher level.

(IV) Under any situation, the Boycott effect cannot be ignored for proppant settling in inclined fractures. Although high fracturing fluid viscosity and proppant with small size and density can prevent rapid settling of proppant in rigorously vertical fractures, the results can change dramatically in inclined fractures. This work shows that decreasing proppant density is an efficient way to lower the absolute averaged settling velocity. However, the results also demonstrate that decreasing proppant size can even increase the absolute averaged settling velocity to some extent.

In this work, we aim to discover the fundamental mechanisms that play important roles during proppant settling in inclined fractures, and many factors are simplified to some extent. For example, fracture width is assumed to be constant in this work. However, width is usually not uniformly distributed for a real fracture, which can lead to a local net flow and affect the developments of instabilities. Uneven particle size distribution should also be considered for real-world proppants. Moreover, the adopted subgrid eddy viscosity model in this work was originally built for pure fluid, which may be not accurate for fluid-particle flow. In future work, we will incorporate these important factors for investigating more complex and real scenarios.

## ACKNOWLEDGMENT

This work is partially funded by the National Natural Science Foundation of China (Grant No. 51520105005).

- 
- [1] T. Peacock, F. Blanchette, and J. W. M. Bush, The stratified Boycott effect, *J. Fluid Mech.* **529**, 33 (2005).
  - [2] F. Blanchette, T. Peacock, and J. W. M. Bush, The Boycott effect in magma chambers, *Geophys. Res. Lett.* **31**, L05611 (2004).
  - [3] R. Tarpagkou and A. Pantokratoras, The influence of lamellar settler in sedimentation tanks for potable water treatment—a computational fluid dynamic study, *Powder Technol.* **268**, 139 (2014).
  - [4] S. Sarkar, D. Kamilya, and B. C. Mal, Effect of geometric and process variables on the performance of inclined plate settlers in treating aquacultural waste, *Water Res.* **41**, 993 (2007).
  - [5] L. R. Kern, T. K. Perkins, and R. E. Wyant, The mechanics of sand movement in fracturing, *J. Pet. Technol.* **11**, 55 (1959).
  - [6] J. Wang, D. Elsworth, and M. K. Denison, Propagation, proppant transport and the evolution of transport properties of hydraulic fractures, *J. Fluid Mech.* **855**, 503 (2018).
  - [7] J. Adachi, E. Siebrits, A. Peirce, and J. Desroches, Computer simulation of hydraulic fractures, *Int. J. Rock Mech. Min. Sci.* **44**, 739 (2007).
  - [8] Z. Yushi, M. Xinfang, Z. Shicheng, Z. Tong, and L. Han, Numerical investigation into the influence of bedding plane on hydraulic fracture network propagation in shale formations, *Rock Mech. Rock Eng.* **49**, 3597 (2016).
  - [9] T. Chun, Y. Li, and K. Wu, Comprehensive experimental study of proppant transport in an inclined fracture, *J. Pet. Sci. Eng.* **184**, 106523 (2020).
  - [10] A. E. Boycott, Sedimentation of blood corpuscles, *Nature* **104**, 532 (1920).
  - [11] E. Ponder, On sedimentation and Rouleaux formation, *Q. J. Exp. Physiol.* **15**, 235 (1925).
  - [12] H. Nakamura and K. Kuroda, La cause de l'accélération de la vitesse de sédimentation des suspensions dans les récipients inclinés, *Keijo J. Med.* **8**, 256 (1937).
  - [13] A. Acrivos and E. Herbolzheimer, Enhanced sedimentation in settling tanks with inclined walls, *J. Fluid Mech.* **92**, 435 (1979).
  - [14] E. Herbolzheimer, Stability of the flow during sedimentation in inclined channels, *Phys. Fluids* **26**, 2043 (1983).
  - [15] Y. A. Nevskii and A. N. Osipov, Slow gravitational convection of disperse systems in domains with inclined boundaries, *Fluid Dyn.* **46**, 225 (2011).
  - [16] S. Sundaresan, A. Ozel, and J. Kolehmainen, Toward constitutive models for momentum, species, and energy transport in gas-particle flows, *Annu. Rev. Chem. Biomol. Eng.* **9**, 61 (2018).
  - [17] Y. Tsuji, Multi-scale modeling of dense phase gas-particle flow, *Chem. Eng. Sci.* **62**, 3410 (2007).
  - [18] J. Zeng, H. Li, and D. Zhang, Direct numerical simulation of proppant transport in hydraulic fractures with the immersed boundary method and multi-sphere modeling, *Appl. Math. Modell.* **91**, 590 (2021).
  - [19] X. Li, Simulation of proppant transport in slickwater with DNS-derived drag correlations, Ph.D. dissertation, Colorado School of Mines, 2018.
  - [20] C. A. J. Blyton, D. P. Gala, and M. M. Sharma, A comprehensive study of proppant transport in a hydraulic fracture, in *Proceedings of the SPE Annual Technical Conference and Exhibition* (Society of Petroleum Engineers, Dallas, TX, 2015), p. 3391.
  - [21] M. A. van der Hoef, M. van Sint Annaland, N. G. Deen, and J. A. M. Kuipers, Numerical simulation of dense gas-solid fluidized beds: A multiscale modeling strategy, *Annu. Rev. Fluid Mech.* **40**, 47 (2008).
  - [22] D. M. Snider, An incompressible three-dimensional multiphase particle-in-cell model for dense particle flows, *J. Comput. Phys.* **170**, 523 (2001).
  - [23] N. A. Patankar and D. D. Joseph, Lagrangian numerical simulation of particulate flows, *Int. J. Multiphase Flow* **27**, 1685 (2001).

- [24] J. Han, P. Yuan, X. Huang, H. Zhang, A. Sookprasong, C. Li, and Y. Dai, Numerical study of proppant transport in complex fracture geometry, in *Proceedings of SPE Low Perm Symposium* (Society of Petroleum Engineers, Dallas, TX, 2016).
- [25] M. Roostaei, A. Nouri, V. Fattahpour, and D. Chan, Numerical simulation of proppant transport in hydraulic fractures, *J. Pet. Sci. Eng.* **163**, 119 (2018).
- [26] A. T. Mobbs and P. S. Hammond, Computer simulations of proppant transport in a hydraulic fracture, *SPE Prod. Facil.* **16**, 112 (2001).
- [27] Z. Y. Zhou, S. B. Kuang, K. W. Chu, and A. B. Yu, Discrete particle simulation of particle-fluid flow: Model formulations and their applicability, *J. Fluid Mech.* **661**, 482 (2010).
- [28] C. T. Crowe, J. D. Schwarzkopf, M. Sommerfeld, and Y. Tsuji, *Multiphase Flows with Droplets and Particles*, 2nd ed. (CRC Press, Boca Raton, FL, 2011).
- [29] A. W. Vreman, An eddy-viscosity subgrid-scale model for turbulent shear flow: Algebraic theory and applications, *Phys. Fluids* **16**, 3670 (2004).
- [30] P. A. Cundall and O. D. L. Strack, A discrete numerical model for granular assemblies, *Geotechnique* **30**, 331 (1980).
- [31] M. W. Schmeeckle, Numerical simulation of turbulence and sediment transport of medium sand, *J. Geophys. Res.: Earth Surf.* **119**, 1240 (2014).
- [32] R. Sun and H. Xiao, SediFoam: A general-purpose, open-source CFD-DEM solver for particle-laden flow with emphasis on sediment transport, *Comput. Geosci.* **89**, 207 (2016).
- [33] K. L. Johnson, *Contact Mechanics* (Cambridge University Press, Cambridge, 1999).
- [34] S. Luding, Cohesive, frictional powders: contact models for tension, *Granular Matter* **10**, 235 (2008).
- [35] M. R. Maxey and J. J. Riley, Equation of motion for a small rigid sphere in a nonuniform flow, *Phys. Fluids* **26**, 883 (1983).
- [36] R. Di Felice, The voidage function for fluid-particle interaction systems, *Int. J. Multiphase Flow* **20**, 153 (1994).
- [37] P. G. Saffman, The lift on a small sphere in a slow shear flow, *J. Fluid Mech.* **22**, 385 (1965).
- [38] L. C. van Rijn, Sediment transport, Part I: Bed load transport, *J. Hydraul. Eng.* **110**, 1431 (1984).
- [39] J. Brady, Stokesian dynamics, *Annu. Rev. Fluid Mech.* **20**, 111 (1988).
- [40] N. Q. Nguyen and A. J. C. Ladd, Lubrication corrections for lattice-Boltzmann simulations of particle suspensions, *Phys. Rev. E* **66**, 046708 (2002).
- [41] R. Sun and H. Xiao, CFD-DEM simulations of current-induced dune formation and morphological evolution, *Adv. Water Resour.* **92**, 228 (2016).
- [42] H. K. Versteeg and W. Malalasekera, *An Introduction to Computational Fluid Dynamics: The Finite Volume Method* (Pearson Education Limited, London, 2007).
- [43] B. P. Leonard, A stable and accurate convective modelling procedure based on quadratic upstream interpolation, *Comput. Methods Appl. Mech. Eng.* **19**, 59 (1979).
- [44] S. V. Patankar and D. B. Spalding, A calculation procedure for heat, mass and momentum transfer in three-dimensional parabolic flows, *Int. J. Heat Mass Transfer* **15**, 1787 (1972).
- [45] <https://www.mcs.anl.gov/petsc>.
- [46] B. Tian, J. Zeng, B. Meng, Q. Chen, X. Guo, and K. Xue, Compressible multiphase particle-in-cell method (CMP-PIC) for full pattern flows of gas-particle system, *J. Comput. Phys.* **418**, 109602 (2020).
- [47] G. R. Liu and M. B. Liu, *Smoothed Particle Hydrodynamics: A Meshfree Particle Method* (World Scientific Publishing, Singapore, 2003).
- [48] P. S. Ergun, Fluid flow through packed columns, *Chem. Eng. Prog.* **48**, 89 (1952).
- [49] M. Wong and G. Parker, Reanalysis and correction of bed-load relation of Meyer-Peter and Muller using their own database, *J. Hydraul. Eng.* **132**, 1159 (2006).
- [50] P. Nielsen, *Coastal Bottom Boundary Layers and Sediment Transport* (World Scientific Publishing, Singapore, 1992).